Geophysical Research Letters

RESEARCH LETTER
10.1029/2022GL100283

Key Points:

- Geodetic imaging, back-projection, multiple point source and finite fault inversions are conducted for the Maduo earthquake
- We show a stable rupture speed (~2.5 km/s) of the entire rupture and a simultaneous rupture through bifurcated fault branches
- The stopping phase on the southern branch likely stopped the rupture on the northern branch

Supporting Information:

Supporting Information may be found in the online version of this article.

Correspondence to:

S. Wei,
shjwei@gmail.com

Citation:

Wei, S., Zeng, H., Shi, Q., Liu, J., Luo, H., Hu, W., et al. (2022). Simultaneous rupture propagation through fault bifurcation of the 2021 Mw7.4 Maduo earthquake. *Geophysical Research Letters*, *49*, e2022GL100283. https://doi.org/10.1029/2022GL100283

Received 6 JUL 2022
Accepted 30 OCT 2022

Author Contributions:

Conceptualization: Shengji Wei
Data curation: Jihong Liu, Heng Luo, Yu Li, Weitao Wang, Zhangfeng Ma, Teng Wang
Formal analysis: Shengji Wei, Hongyu Zeng, Qibin Shi
Funding acquisition: Shengji Wei
Investigation: Shengji Wei
Methodology: Shengji Wei, Hongyu Zeng, Qibin Shi
Project Administration: Shengji Wei
Resources: Shengji Wei
Software: Shengji Wei, Hongyu Zeng, Qibin Shi, Jihong Liu
Supervision: Shengji Wei
Validation: Shengji Wei, Hongyu Zeng, Qibin Shi, Jihong Liu, Heng Luo, Yu Li
Visualization: Shengji Wei, Hongyu Zeng, Qibin Shi, Wanlin Hu
Writing – original draft: Shengji Wei

Simultaneous Rupture Propagation Through Fault Bifurcation of the 2021 Mw7.4 Maduo Earthquake

Shengji Wei[1,2], Hongyu Zeng[2], Qibin Shi[1], Jihong Liu[3], Heng Luo[4], Wanlin Hu[2], Yu Li[5,6], Weitao Wang[5], Zhangfeng Ma[2,7], Jing Liu-Zeng[8], and Teng Wang[4]

[1]Earth Observatory of Singapore, Nanyang Technological University, Singapore, Singapore, [2]Asian School of the Environment, Nanyang Technological University, Singapore, Singapore, [3]School of Geosciences and Info-Physics, Central South University, Changsha, China, [4]School of Earth and Space Sciences, Peking University, Beijing, China, [5]Institute of Geophysics, China Earthquake Administration, Beijing, China, [6]China Earthquake Networks Center, China Earthquake Administration, Beijing, China, [7]School of Earth Sciences and Engineering, Hohai University, Nanjing, China, [8]School of Earth System Science, Tianjin University, Tianjin, China

Abstract Fault geometric complexity plays a critical role in earthquake rupture dimension. Fault bifurcations are commonly observed in earthquake geology, yet, robust kinematic rupture processes on bifurcated fault branches are largely missing, limiting our understanding of rupture dynamics and seismic hazard. Here, we holistically study the fault geometry and bilateral rupture of the 2021 Mw7.4 Maduo, China earthquake, that shows clear fault bifurcation near its eastern terminal. We integrate space geodesy imaging, back-projection of high-frequency teleseismic array waveforms, multiple point source and finite fault inversions, and constrain in detail the rupture process, in particular, through its fault bifurcation. Our models reveal a stable rupture speed of ~2.5 km/s throughout the entire rupture and a simultaneous rupture through fault branches bifurcated at 20°. The rupture on bifurcated faults radiated more high-frequency waves, especially from the stopping phases. The stopping phase on the southern branch likely stopped the rupture on the northern branch.

Plain Language Summary Earthquake is produced by sudden shear dislocation across the fault. The geometric complexity of fault structure, such as bend, step-over, branching and bifurcation, play important roles in determining the final rupture dimension (hence the magnitude) of the earthquake, as they can easily produce stress heterogeneity on the faults. Although geological and recent space geodetic observations have well-recorded the fault geometry complexity, detailed spatial and temporal evolution of rupture through such fault segments, especially fault bifurcations, are rarely well-imaged. In this study, we integrate broadband seismic waveform and geodetic observations for the 2021 Mw7.4 Maduo earthquake in China, and process and model them with a set of tools, to produce a high resolution rupture model for the earthquake. The preferred model reveals a near constant rupture speed of 2.5 km/s throughout the entire rupture, and resolves the detailed rupture process through the bifurcated fault segments at its eastern terminal, where the termination of the rupture on the southern branch stopped the rupture on the northern branch.

1. Introduction

Fault bends, branches, and step-overs play critical roles in the nucleation, propagation, and termination of earthquake ruptures (Ji et al., 2003; King & Nábělek, 1985; Qiu et al., 2016; Wesnousky, 2006). Fault branching and bifurcation are commonly observed for strike-slip earthquakes in fault mapping (e.g., Sieh et al., 1993) and more recently in high-resolution space geodesy images (e.g., Wei et al., 2011). To explain these observations, structure evolution models (Wesnousky, 1988, 2008), theorical analysis (Poliakov et al., 2002), dynamic simulation models (Kame et al., 2003), as well as lab experiments (Templeton et al., 2009) have been proposed. It has been shown that prestress conditions, rupture speed, and bifurcation angle all impact rupture evolution through fault branching and bifurcation (Aochi et al., 2002; Douilly et al., 2020; Duan & Oglesby, 2007; Kame et al., 2003; Poliakov et al., 2002). These theorical and numerical modeling results show a wide spectrum of rupture scenarios. However, to date, to the best of our knowledge, the details of kinematic rupture processes of such fault bifurcation and branching have not been reported. This may be partially accounted for by the fact that the slip on these faults is relatively small compared with the largest slip patches of the rupture, and seismological inversions are usually dominated by the larger slip patches, unless very near-fault seismic observations are available (Ji et al., 2003).

Writing – review & editing: Shengji Wei, Hongyu Zeng, Qibin Shi, Jihong Liu, Jing Liu-Zeng, Teng Wang

The left-lateral strike-slip Mw7.4 Maduo earthquake occurred on 21 May 2021, rupturing the near E-W oriented JiangCuo fault, which is located within the Bayan Har block (Zhan et al., 2021) in the northeastern Tibetan Plateau (Figure 1b). The earthquake was well-recorded in space geodetic images (He et al., 2022; J Liu et al., 2022) and nearby static (M. Wang, Wang, et al., 2022) and high-rate Global Positional System (GPS) offsets (Gao et al., 2021). Earlier reports of the earthquake show that this was a bilateral rupture, which propagated ∼80 km to both sides of the epicenter (He et al., 2022; Ren et al., 2022; S. Wang, Song, et al., 2022). While (Chen et al., 2022) d erived a stable rupture speed of ∼2.5 km/s for the entire rupture, (Zhang et al., 2022) and (Lyu et al., 2022; Yue et al., 2022) reported a supershear speed for rupture toward the east. Recently, (Li et al., 2022) also reported asymmetric rupture velocities for the earthquake with a holistic approach. Although various analyses have been reported for the earthquake, a comprehensive investigation is still missing to resolve the kinematic rupture details at its eastern end that shows clear fault bifurcation but reported with different rupture speeds. To constrain the rupture details of the earthquake, here we adopt various data processing techniques and kinematic inversion methods that cover a wide range of observations. We pay special attention to the fault bifurcation and its seismic wave radiation, thus aiming to shed new light on earthquake physics.

2. Geodetic Observations

We process Sentinal-1 and Advanced Land Observation Satellite-2 (ALOS-2) Synthetic Aperture Radar (SAR) data (Table S1 in Supporting Information S1) to derive 11 surface deformation images through DInSAR (differential interferometric SAR) (Gabriel et al., 1989), pixel offset tracking (Michel et al., 1999), multiple aperture interferometry (Bechor & Zebker, 2006), and/or burst overlap interferometry (Grandin et al., 2016) methods (Figure S1 in Supporting Information S1). These images provide high-quality and comprehensive spatial coverage of the surface deformation produced by the earthquake. We then use them to calculate the 3D co-seismic displacement with the Strain Model and Variance Component Estimation method (J. Liu et al., 2019; J.-H. Liu et al., 2017) (Text S1 in Supporting Information S1). The high-resolution 3D surface deformation shows sharp offsets across the fault, thus the surface rupture, continuously along the near E-W oriented Jiangcuo fault (Figure 1b and Figure S2 in Supporting Information S1), which agrees well with the surface rupture mapping from field surveys (Ren et al., 2022). The total surface rupture length is ∼160 km, ∼60 km longer than that predicted from empirical relationships (Leonard, 2010; Wells & Coppersmith, 1994), suggesting a relatively shallow rupture of the earthquake. The coseismic deformation is dominated by left-lateral strike-slip motion (Figure 1a), and shows at least five primary step-overs or fault bends (strike change >10°) and one fault bifurcation. The refined hypocenter of the mainshock (W Wang et al., 2021) is located in the middle of the surface rupture trace very close to one of the primary fault step-overs, where stress concentrations usually nucleate an earthquake rupture (King & Nábělek, 1985). Interestingly, the epicenter is co-located with the intersection between the Yellow River and the ruptured JiangCuo fault (Figure 2a), although their relationship is not yet clearly understood. Larger surface deformation is observed to the east of the epicenter, and therefore a stronger rupture directivity effect is expected toward the east. Coseismic offsets are clearly observed across the bifurcated fault branches near its eastern terminal (Figure 1a).

3. Fault Geometry and Finite Fault Inversion

We use the geodetic observations and the relocated aftershocks (W Wang et al., 2021) to define the geometry of rectangular fault segments that will be used in the finite fault model (FFM) inversion. Ten fault segments are needed to mimic the first-order strike variations due to bending and bifurcation, as shown in the geodetic observation (Figures 1a and 2a). These 10 segments are sub-vertical faults, as aftershocks are distributed quite close to the surface rupture trace (Figure 2b), and the E-W deformations across the fault are nearly symmetric (Figure 1b). Aftershocks are located mostly to the north of surface rupture at fault segments 1–6 while aftershocks are distributed primarily to the south of surface rupture at fault segments 7–10. Based on this relative location between seismicity and surface rupture trace, we set the dipping direction of fault segments 1–6 and 7–10 toward north and south, respectively (Figure 2). Note, that the seismic stations used in earthquake relocation study are distributed quite uniformly in the source region (W. Wang et al., 2021). Therefore, we can rule out the systematic location bias between the seismicity to the west and east of the epicenter. Geodetic-only inversions can then be conducted to determine the dip angle of each fault segment (Table S2 in Supporting Information S1).

10.1029/2022GL100283

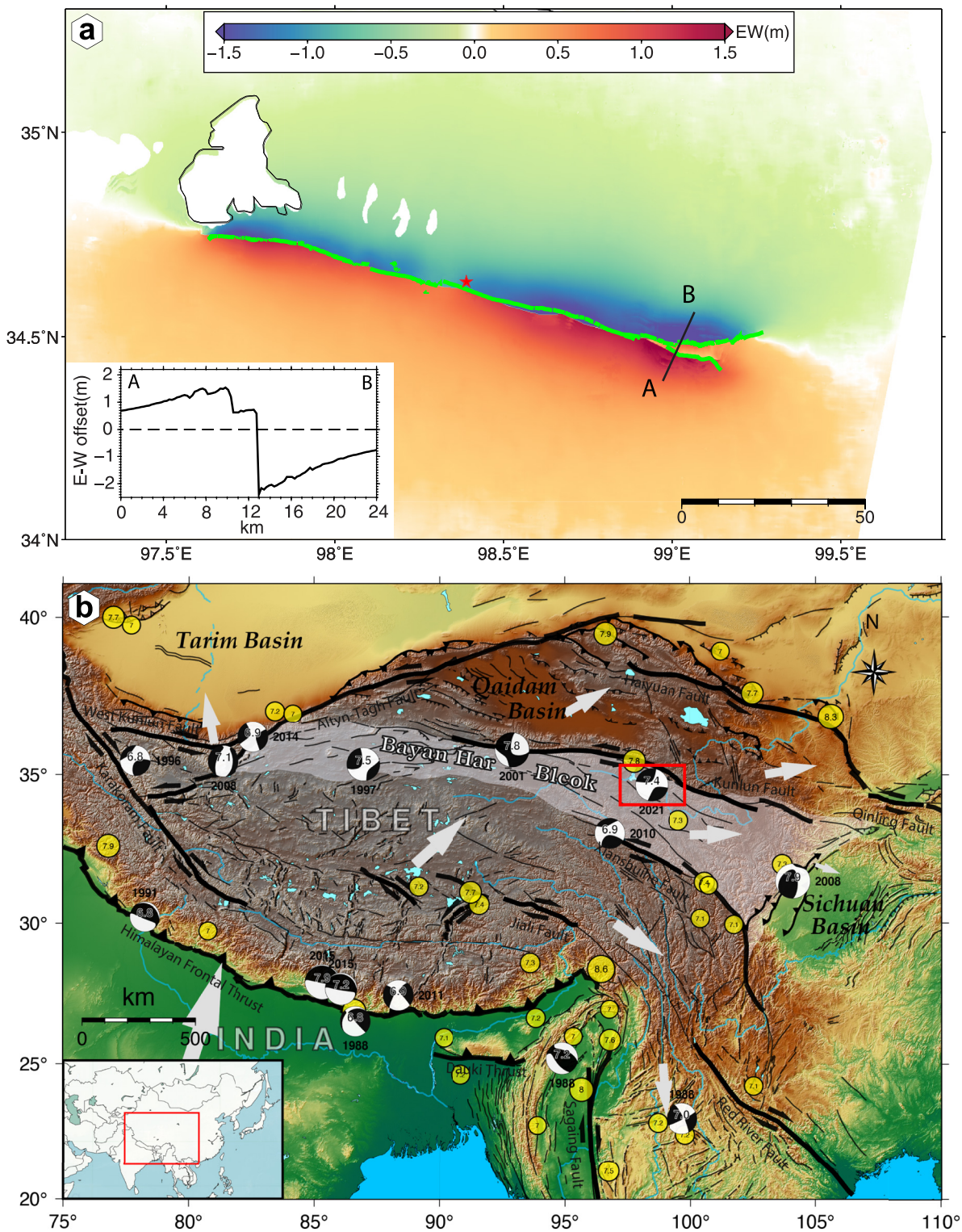

Figure 1. Regional tectonics and surface deformation. (a) E-W component of the 3D surface deformation derived from space geodetic observations. The green lines indicate the surface rupture mapped by Ren et al. (2022), where the step-overs are mostly smaller than 2 km. The inset shows the offset along the profile A-B. (b) Regional tectonics with major strike-slip and thrust faults indicated by the heavy black lines. Earthquake moment tensor for Mw > 6.5 earthquakes in 1990–2022 are shown as beach balls, along with magnitude and year of the event. Historical $M > 7.0$ earthquakes in the last 100 years are displayed as yellow circles. 2022 Mw7.4 Maduo earthquake is highlighted by the red rectangle, defined as the same area as in (a).

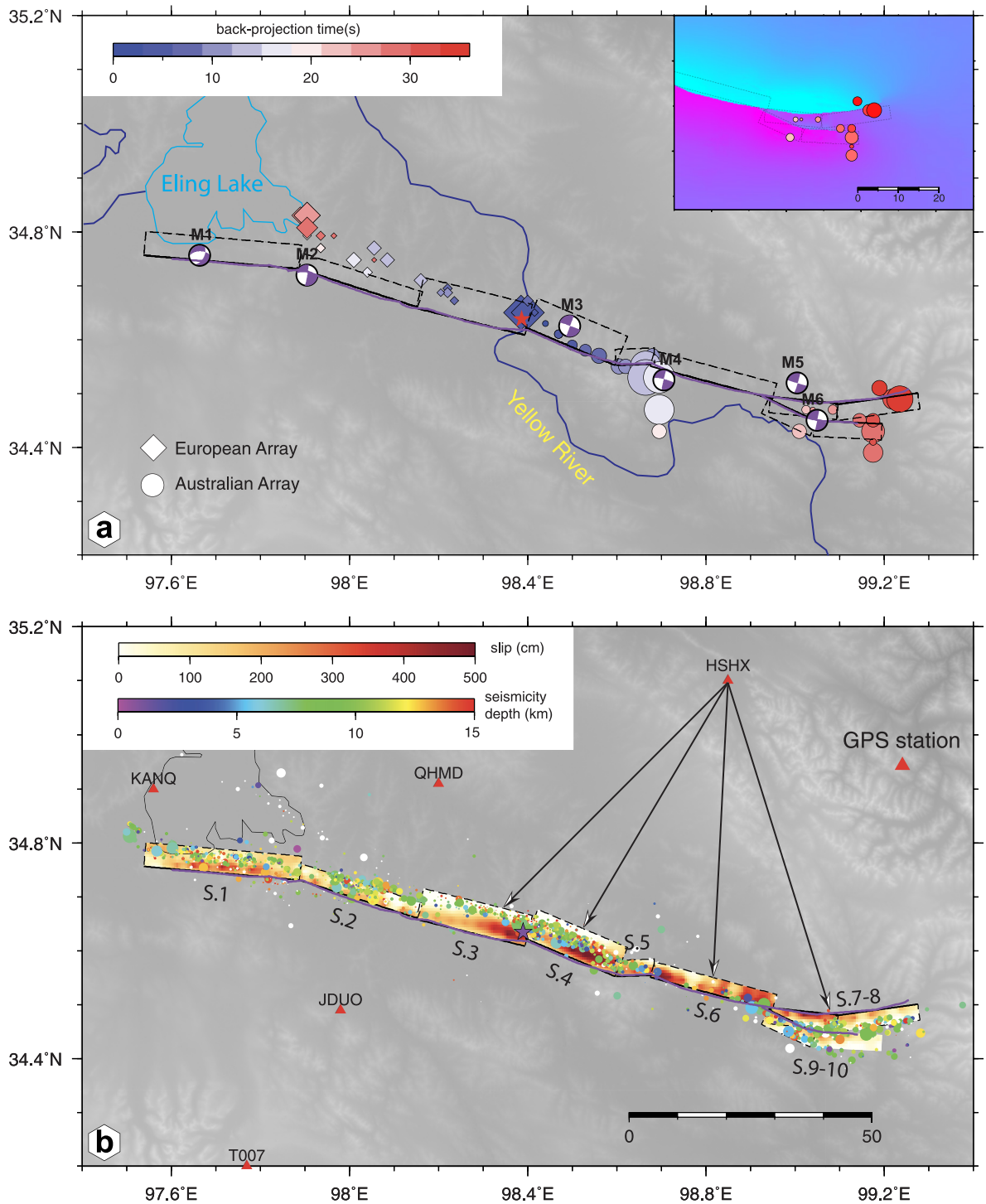

Figure 2. (a) Map view of the back-projection (BP) results derived from European Array (diamond) and Australian array (circles). Surface rupture trace is indicated by the purple line. Rectangles show the surface projection of the fault segments used in finite fault model (FFM) inversion. Multiple point source solutions are indicated by beach balls with the sub-event identity. The inset shows the E-W component of the 3D surface deformation at the eastern terminal of the rupture, along the BP result. (b) Map view of the slip model, displayed with the relocated aftershocks (W. Wang et al., 2021) that are colored by their depth. Circles are proportional to the magnitude of the aftershock. Fault segment numbers used in FFM inversion are indicated as S1–S10. Triangles indicate the high-rate Global Positional System stations that are used in the FFM inversion. The arrows connected to station HSHX roughly show the distance differences from the station to various fault segments.

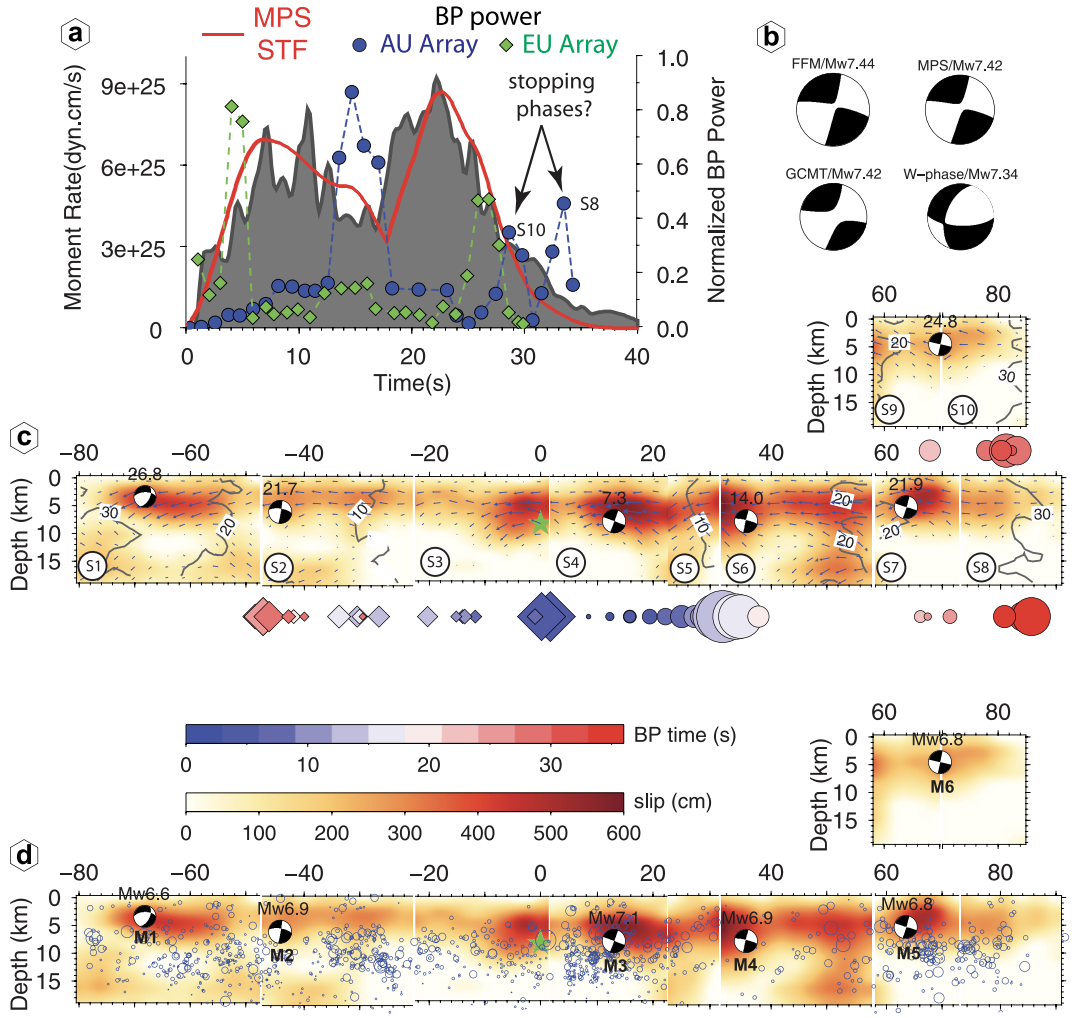

Figure 3. Dynamic rupture models. (a) Shaded curve represents the moment-rate function of finite fault model (FFM), summed source time function of multiple point source (MPS) solution is indicated by the red line, and back-projection (BP) power from Australian array (circle) and European array (diamond). (b) Equivalent moment-tensors of FFM and MPS solutions, along with that reported from Global Centroid Moment Tensor (GCMT) and W-phase catalogs. (c) Depth profile of the rupture model with the green star shows the hypocenter. Segment numbers are indicated in the lower left corner of each segment (see Figure 2 for their map view). Blue arrows show the rake angle of each sub-fault and contour lines indicate the rupture time. The beach balls represent the MPS solution with the number above indicating the centroid time of the sub-event. BP results are displayed below, with the same legend as shown in Figure 2. (d) Depth profile of slip model displayed with the aftershocks (blue open circles) and MPS solution (beach balls). The moment magnitude (above) and sub-event identity (below) are shown with the beach balls.

Based on this fault geometry, we jointly invert geodetic data, nearby high-rate GPS waveforms, regional broadband waveforms and teleseismic body waves using a finite fault inversion method (Ji et al., 2002) to recover the kinematic rupture history and slip distribution on the fault segments (Text S2 in Supporting Information S1). We divide the rectangular fault segments into 3 × 2 km patches, and invert for the slip amplitude, slip direction, rupture time and rise time on each patch. A Laplacian smoothing algorithm is applied for the slip distribution during the inversion. High-quality nearfield geodetic and high-rate GPS observations greatly suppress the trade-offs between the parameters in the inversion. The best average rupture speed and static weight are determined through a grid search way (Figure S3 in Supporting Information S1).

Our preferred FFM is presented in Figure 2b in a map view and in Figure 3 as a depth view along the strike. This model produces excellent fits to both seismic waveforms (Figure S4–S6 in Supporting Information S1) and static surficial deformations (Figure S7–S9 in Supporting Information S1), suggesting a reliable model resolution,

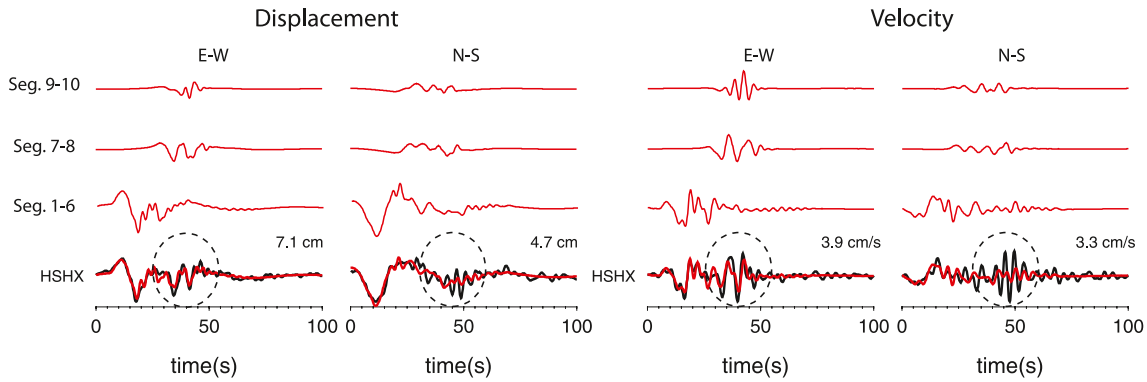

Figure 4. Waveform fits of the horizontal components for high-rate Global Positional System station HSHX in displacement (left) and velocity (right), with the synthetics in red and data in black. All the waveforms are filtered to 0.02–0.4 Hz. Peak amplitude of the data is indicated at the end of each waveform pair. Synthetic waveforms are decomposed into the contributions from Seg.1–6, Seg.7–8, and Seg. 9–10. Dashed circles highlight the waveform segments that show different relative amplitude to the earlier rupture between displacement and velocity waveforms.

which is further supported by individual data set inversions and sensitivity tests (Figure S10–S12 in Supporting Information S1). Most of the slips are distributed at the depth shallower than 8 km except for S5 and S6, where slips are as deep as 15 km. Interestingly, the distribution of the aftershocks also shows a gap at S5 and S6 (Figures 2b and 3d), indicating the rupture released most of the stress accumulated in the entire seismogenic zone, which has a depth of ∼15 km. On the other segments, where the seismogenic zone is only partially ruptured, aftershocks are much denser, and distributed in the depth range of 5–15 km, showing a clear complementary feature with the coseismic slip distribution (Figure 3d), similar to that observed for other strike-slip earthquakes (e.g., Wei et al., 2011). The aftershocks were most likely triggered by down-dip post seismic slip and Coulomb stress change imposed by coseismic slip. Therefore, slip deficit happens both at shallow (Jin & Fialko, 2021) and at greater depths, that is, at the upper and lower bounds of the seismogenic zone. The equivalent moment tensor of the FFM shows relatively small non-double-couple component (Figure 3b), which is highly similar to that from multiple point source (MPS) solution (see next section). Our equivalent moment tensors are more similar to the Global Centroid Moment Tensor solution, including the Mw, but much more different from the W-phase solution, in which the east-west oriented fault plane has a shallower dip angle (67°) and quite strong normal faulting component in rake (−40°). It appears that a reliable FFM of Maduo earthquake provides an independent verification to the global moment tensor solutions.

There are substantial slip distributions on the two branches of the bifurcated fault, where the moment magnitude of the northern branch (S7–S8, Mw6.8) is slightly larger than that on the southern branch (S9–S10, Mw6.7). The sizable and comparable moment distribution on the two branches is a key feature that allows robust resolution on their ruptures. The waveform observations on high-rate GPS station HSHX exhibit a clear frequency-dependent feature that the rupture from the bifurcated branches (S7–S10) produced more high-frequency seismic waves than that from earlier ruptures (S1-6) (Figure 4). HSHX station is located at almost the same distances away from S4 to S10 (Figure 2b), therefore the geometric spreading induced attenuations at HSHX are similar for ruptures on these fault segments. If we assume pure strike-slip motion uniformly distributed on these fault segments, we would expect stronger seismic waves from S4 to S6 as the azimuth of HSHX is closer to the strongest SH-wave radiation direction of S4–S6. Indeed, in the displacement waveforms, which are dominated by low-frequency energy, seismic waves excited from S1 to S6 show larger amplitudes than those fromS7 to S10, as shown in the synthetic waveform decompositions (Figure 4). However, in velocity waveforms, in which higher-frequency features are presented, the waveform amplitudes from S7 to S10 are larger than those from S1 to S6. This suggests that S7–S10 radiated more high-frequency waves than those on the other fault segments. Note that the displacement waveforms are dominated by the periods of 10–20 s, while the velocity waveforms show stronger energy at 5–10 s. We did not fit the N-S velocity waveform as good as the E-W component for the rupture from S7 to S10 (highlighted by circles in Figure 4). This portion of the waveform shows more high frequency energy in the N-S component than the E-W component. This larger misfit to the higher frequency waveform is likely because our FFM inversion is dominated by relatively low frequency energy in the observations.

4. Multiple Point Source Solution

The key rupture characteristics of the Maduo earthquake are further confirmed at the intermediate frequency bands, with a MPS inversion method (Q Shi et al., 2018) using high-rate GPS waveforms, regional broadband waveforms, and teleseismic body waves (Figure S13 in Supporting Information S1) (Text S3 in Supporting Information S1). An MPS solution usually uses 2–10 pure dislocation point sources to approximate the complex fault geometry and the rupture process of a large earthquake (e.g., Duputel et al., 2012). Compared with a FFM, a smaller number of MPS parameters can resolve the most robust earthquake rupture features at 0.2 Hz and lower frequencies for the Maduo earthquake. In this frequency range, we find that 6-point sources (M1–M6, Table S3, Figure S13–S18 in Supporting Information S1) are needed to adequately approximate the first order geometry and rupture complexity of the earthquake.

Our preferred MPS solution is presented as beach balls in map view (Figure 2) and depth profiles (Figure 3), with M1–M2 and M3–M6 located to the west and east of the epicenter, respectively. Uncertainty distributions of the solution (Figures S14–S15 and S17 in Supporting Information S1) show that the location, starting time, length and shape of the source time function, and focal mechanism parameters are well resolved (Figure S18 in Supporting Information S1), mostly owing to the constraints of nearby high-rate GPS observations. Figure S16 in Supporting Information S1 presents the decomposition of synthetics from each sub-events in fitting the closest high-rate GPS stations, which demonstrates the sensitivity and variation of the contributions from different stations. The centroid depths of M3 (7.8 km) and M4 (7.8 km) correspond to deep ruptures on fault segments S4–S6, while M1, M2, M5, and M6 (3–6 km) indicate relatively shallow ruptures. This is highly consistent with the FFM slip distribution (Figure 3). The summation of source time functions from the MPS solution also highly resembles the FFM moment-rate function, except for several high-frequency features, which is expected, as we use lower-frequency waves in the MPS inversion. Interestingly, M5 and M6 are located on the northern and southern branches of the fault bifurcation, respectively. The strike of E-W oriented fault plane of M5 is ∼10° counter-clockwise to the strike of M6 (Figure S15 in Supporting Information S1), roughly consistent with the strike difference between the two fault branches. The source durations of M5 and M6 are shorter than those of the other sub-events (Figure S14b in Supporting Information S1), as also shown in the waveform decomposition in fitting the closest high-rate GPS data, where M5 and M6 show sharper pulse in fitting the later portion of E-W component at HSHX station (Figure S16 in Supporting Information S1). This shorter source time function feature is in line with more high-frequency energy radiation from the bifurcation rupture as revealed by the FFM model and the following back-projection (BP) analysis.

5. Back-Projection Rupture Process Imaging

To resolve its high frequency radiation and the rupture speed of the Maduo earthquake independent from FFM and MPS solutions, we perform a MUltiple SIgnal Classification BP analysis (Meng et al., 2011; Zeng et al., 2020) using high-frequency (0.3–1.0 Hz) teleseismic P-waves recorded by the European array (EU) and Australian array (AU) (Text S4 in Supporting Information S1). To take into account the potential impact of the 3D source-side velocity structure on the travel time, we apply a path calibration algorithm using the arrival times of mainshock and other nearby events, which was proved to be necessary for more accurate BP analysis (Zeng et al., 2022). The effectiveness of the calibration is verified by applying it to the BP analysis of the $M > 5$ aftershocks. We compare the differences between the BP locations and the refined epicenter locations for these events (W Wang et al., 2021). Note that our calibration events include the earthquakes away from the mainshock rupture zone (Figure S19 in Supporting Information S1), such selection was shown to be more accurate for travel time error interpolation (Zeng et al., 2022). After trying different groups of calibration events, it appears that we need to use different calibration event combinations to obtain high consistency between the calibrated BP locations and the refined epicenters for the events located to the east and west of the mainshock epicenter, respectively (Figure S19–S20 in Supporting Information S1). This calibration strategy works well for the EU and AU arrays, as they can only resolve the rupture directivity toward west and east, respectively, likely due to the Doppler effect from rupture directivity. We consider the average difference between the BP locations and epicenters as the location uncertainty of BP results, which is 7.5 km for AU array and 4.5 km for the EU array.

Using this path-calibrated BP method, we derive the spatial and temporal evolution of the mainshock rupture using EU and AU arrays. The results are presented as location of high-frequency radiators colored by their timing

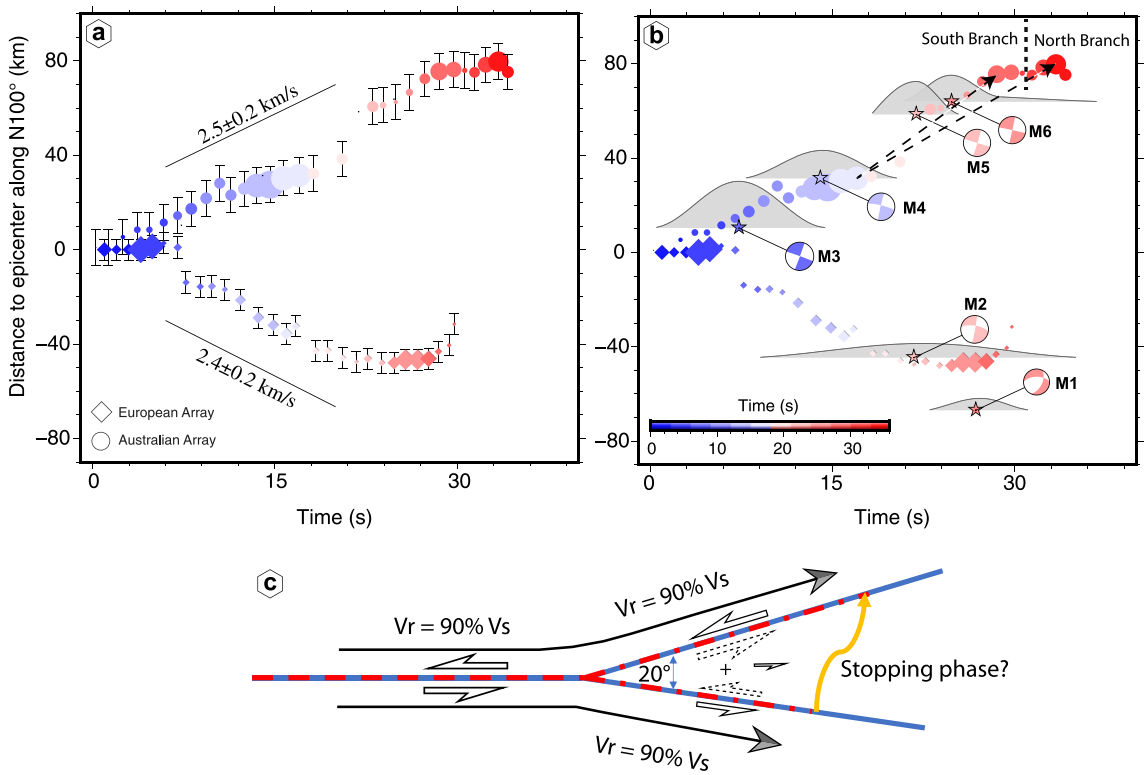

Figure 5. Rupture speed estimation from back projection and multiple point source (MPS) inversion results. (a) Spatial and temporal distribution of the high frequency radiators derived from European array (diamonds) and Australian array (circles), plotted relative to the epicenter location and time. Two straight lines indicate the approximated averaged rupture speed toward east and west of the epicenter. Vertical bars are the spatial errors of the back-projection (BP) results (see Supporting Information S1 for more details). (b) Overlaps of the BP and MPS results. Stars are the centroid location of subevents in MPS solution. Shaded curves represent the source time function of each subevent, both the stars and beach balls are colored by the centroid time. The dashed line separates the high frequency radiators from the north and south branches of the bifurcation rupture. Since the location and time of MPS solution agree well with BP results, we consider the rupture speeds derived from MPS solution are the same as that from BP results. (c) A schematic cartoon shows the rupture (red lines) propagation through the fault bifurcation. The sandwiched/wedge block shows small eastward displacement because of the opposite motions from the rupture on the northern and southern fault segments.

(Figure 2a). BP results from the EU array reveal only the rupture directivity toward the west, and the results from the AU array show only rupture directivity toward the east. The locations of the BP results are mostly less than 10 km away from the surface rupture, suggesting reliable solutions. The location of the large amplitude high-frequency radiators are highly correlated with the fault bends or step-overs (Figure 2a), which also mark the boundaries of fault segments (Figure 3c). This is because stress is usually concentrated at fault kinks and bends (King & Nábělek, 1985), where coseismic slip distribution shows larger gradients (e.g., Figure 3d). Such complementary feature between BP result and slip distribution also presents in the moment-rate versus BP power plot (Figure 3a), where the peaks of BP power always locate at the edges of moment-rate peaks.

With the timing and location of the high-frequency radiators, the rupture speed of the earthquake can be derived (Figure 5), which shows a speed of 2.4 km/s toward the west and of 2.5 km/s toward the east. These rupture speeds are quite stable throughout the rupture and highly consistent with the result from FFM and MPS inversions. Given that the shallow part (<6 km, where most of the slip took place) of the crust has a shear wave (Vs) velocity of 2.7 km/s (Zhu & Helmberger, 1996), these rupture speeds are roughly 90% of Vs speed, that is, of the Rayleigh wave speed. Note, that to the west of the fault bifurcation, the BP results show a gap that almost overlaps with the gap in the aftershock seismicity (Figure 3). The coseismic rupture of this fault segment is deeper, as shown on fault segment S6 in the FFM, and smoother, as shown in the waveform decomposition (Figure 4), than the rupture on the other fault segments. Such a smoother rupture could be explained as more uniform stress distribution and/or smoother fault geometry (Z. Shi & Day, 2013). As the rupture propagated through the junction of bifurcation, high-frequency radiators started to appear on both fault branches, with their amplitudes increasing gradually as the rupture propagated on each of the fault branch (Figure 2a). Enhanced higher-frequency radiation from the bifurcated fault branches (segments S7–S10) is consistent with the waveform decomposition analysis of the

high-rate GPS data recorded at HSHX station (Figure 4 and Figure S12 in Supporting Information S1). But note, that GPS velocity waveforms are dominated by the ∼0.2 Hz energy, while the BP results are derived at ∼1.0 Hz. It is interesting to see that the largest amplitude of high-frequency radiators on the bifurcated fault branches are located at the end of each fault branch (Figure 2a inset). The timings of these peaks are also consistent with the end of the rupture time, as shown in both the MPS source time function and FFM moment-rate function (Figure 3a). Therefore, we propose that the large amplitude high-frequency radiators on each fault branch were produced by the stopping phase of the rupture (Savage, 1965). Rupture on the southern branch (S10) stopped ∼5s earlier than the rupture on the northern branch (S8) (Figures 3a and 5b). As shown in the surface deformation image (Figure 2a), the distance between the rupture tips on the two fault branches is ∼15 km, which corresponds to ∼5s for the S-wave of the stopping phase to travel between the two fault tips. It is therefore likely that the stopping phase on the southern branch (S10), which produced negative Coulomb stress change on the northern branch (S8), therefore stopped the rupture on S8. From the timing and location of the BP results, we show that the rupture propagated simultaneously on the two branches of the bifurcation.

6. Discussion

We note that (Li et al., 2022) also presents a holistic study on the rupture of the Maduo earthquake by using FFM and MPS inversions, as well as BP analysis. Here we highlight several key differences between our study and theirs. (a) In our FFM inversion, we use regional broadband and near fault high-rate GPS waveform data, which were not used in Li et al. (2022). These datasets are critical to constrain the kinematic rupture details of the earthquake. (b) Our MPS inversion does not have any prior constraints on any of the source parameters, but the MPS inversion in Li et al. (2022) assumed a constant rupture speed of 2.3 km/s and constrained the location of source to be along the surface rupture trace. In addition, regional broadband and high rate GPS waveforms were not used in their inversion. (c) The BP conducted in our study has been calibrated by the aftershocks to account for the source-side 3D velocity structure effect, such calibration was not performed in Li et al. (2022). We showed in the aftershock BP relocation (Figure S20 in Supporting Information S1), as well as in Zeng et al. (2022) that, such path calibration is needed for higher resolution BP results.

Multiple datasets and results derived from various inversion methods show that the 2021 Maduo earthquake ruptured simultaneously on the two branches of the fault with a branching angle of ∼20°. However, numerical simulations suggest that simultaneous rupturing on both fault branches is usually difficult where the branching angle is narrow, due to strong stress interactions between faults (Aochi & Fukuyama, 2002; Kame et al., 2003). The dynamic stress interaction (or dynamic rupture weakening) plays an important role during earthquake ruptures. Given the stress shadow imposed by the rupture on the other fault branch, rupture through a fault bifurcation that has a narrow branching angle is most likely be simultaneous. Suppose that one of the fault branches ruptures earlier; then the Coulomb stress change on the other fault segment will prohibit its rupture. Only when the ruptures propagate simultaneously through the two fault branches (e.g., Figure 5c), back and forth slip of the fault segments could be avoided. Because the two sides of the wedge block have opposite slip directions (Figure 5c), the final dislocation of this block is smaller than that to the north and south of the block (e.g., Figure 1a inset). Numerical simulations also suggest that a simultaneous rupture is promoted when the friction coefficients are low (Aochi et al., 2002). However, we observe more high-frequency radiation from the bifurcated fault branches, which indicates rougher fault friction. More high-frequency energy released on the branched faults could also be an indication of more energy dissipation, which could eventually lead to the termination of the rupture. Also note, that the bifurcated fault branches are located within slightly higher mountain ranges, suggesting the rupture could have propagated from one geological unit to another (Ren et al., 2022), which could also be a reason for different fault friction.

The rupture speed of the Maduo earthquake was quite stable around 2.5 km/s, which is in contrast with supershear rupture speed derived from the other BP analysis (Yue et al., 2022; Zhang et al., 2022). The primarily reason for this discrepancy could be that we applied travel time path calibrations (see more details in Zeng et al. (2022)) but the other BP studies did not. The rupture did not slow down at the bends and step-overs. This is because all bends/step-overs are releasing bends/step-overs, therefore normal stress decreased when rupture propagated through them, and facilitating the rupture pass-through. Fault bifurcations with narrow branching angle are quite common for strike-slip earthquakes (Figure S21 in Supporting Information S1). The number of fault segments and fault segment length of the Maduo earthquake, including the bifurcated branches, fit well with statistics

from Klinger (2010). We therefore suggest that such simultaneous ruptures of the bifurcated fault branches could be common during strike-slip earthquakes. Dynamic simulations have to take into consideration complex fault geometry, specific stress conditions, and frictional heterogeneities to properly estimate the relationship between rupture through multiple fault segments.

Conflict of Interest

The authors declare no conflicts of interest relevant to this study.

Data Availability Statement

The seismic data used in this study can be downloaded from the II (https://doi.org/10.7914/SN/II) and IU (https://doi.org/10.7914/SN/IU) networks in Incorporated Research Institutions for Seismology (IRIS) through its Wilber3 service (http://ds.iris.edu/wilber3/find_event). Seismic and geodetic datasets used in the inversion can also be downloaded from NTU data repository: https://doi.org/10.21979/N9/NOKYXP.

Acknowledgments
This research was supported by Singapore MOE project (MOE2019–T2–1–182) and the Earth Observatory of Singapore via its funding from the National Research Foundation Singapore and the Singapore Ministry of Education under the Research Centers of Excellence initiative. This work comprises EOS contribution number 445.

References

Aochi, H., & Fukuyama, E. (2002). Three-dimensional nonplanar simulation of the 1992 Landers earthquake. *Journal of Geophysical Research*, *107*(B2), ESE4-1–ESE4-12. https://doi.org/10.1029/2000jb000061

Aochi, H., Madariaga, R., & Fukuyama, E. (2002). Effect of normal stress during rupture propagation along nonplanar faults. *Journal of Geophysical Research*, *107*(B2), ESE5-1–ESE5-10. https://doi.org/10.1029/2001jb000500

Bechor, N. B. D., & Zebker, H. A. (2006). Measuring two-dimensional movements using a single InSAR pair. *Geophysical Research Letters*, *33*(16), 275–303. https://doi.org/10.1029/2006gl026883

Chen, K., Avouac, J. P., Geng, J., Liang, C., Zhang, Z., Li, Z., & Zhang, S. (2022). The 2021 Mw 7.4 Madoi earthquake: An archetype bilateral slip-pulse rupture arrested at a splay fault. *Geophysical Research Letters*, e2021GL095243. https://doi.org/10.1029/2021GL095243

Douilly, R., Oglesby, D. D., Cooke, M. L., & Hatch, J. L. (2020). Dynamic models of earthquake rupture along branch faults of the eastern San Gorgonio Pass region in California using complex fault structure. *Geosphere*, *16*(2), 474–489. https://doi.org/10.1130/ges02192.1

Duan, B., & Oglesby, D. D. (2007). Nonuniform prestress from prior earthquakes and the effect on dynamics of branched fault systems. *Journal of Geophysical Research*, *112*(B5), B05308. https://doi.org/10.1029/2006jb004443

Duputel, Z., Kanamori, H., Tsai, V. C., Rivera, L., Meng, L., Ampuero, J.-P., & Stock, J. M. (2012). The 2012 Sumatra great earthquake sequence. *Earth and Planetary Science Letters*, *351*, 247–257. https://doi.org/10.1016/j.epsl.2012.07.017

Gabriel, A. K., Goldstein, R. M., & Zebker, H. A. (1989). Mapping small elevation changes over large areas: Differential radar interferometry. *Journal of Geophysical Research*, *94*(B7), 9183–9191. https://doi.org/10.1029/JB094iB07p09183

Gao, Z., Li, Y., Shan, X., & Zhu, C. (2021). Earthquake magnitude estimation from high-rate GNSS data: A Case study of the 2021 Mw 7.3 Maduo earthquake. *Remote Sensing-Basel*, *13*(21), 4478. https://doi.org/10.3390/rs13214478

Grandin, R., Klein, E., Métois, M., & Vigny, C. (2016). 3D displacement field of the 2015 M w 8.3 Illapel earthquake (Chile) from across- and along-track Sentinel-1 TOPS interferometry. *Geophysical Research Letters*, *43*(6), 2552–2561. https://doi.org/10.1002/2016GL067954

He, K., Wen, Y., Xu, C., & Zhao, Y. (2022). Fault geometry and slip distribution of the 2021 M w 7.4 Maduo, China, earthquake inferred from InSAR measurements and relocated aftershocks. *Seismological Society of America*, *93*(1), 8–20. https://doi.org/10.1785/0220210204

Ji, C., Helmberger, D. V., Wald, D. J., & Ma, K. F. (2003). Slip history and dynamic implications of the 1999 Chi-Chi, Taiwan, earthquake. *Journal of Geophysical Research*, *108*(B9). https://doi.org/10.1029/2002jb001764

Ji, C., Wald, D. J., & Helmberger, D. V. (2002). Source description of the 1999 Hector Mine, California, earthquake, part I: Wavelet domain inversion theory and resolution analysis. *Bulletin of the Seismological Society of America*, *92*(4), 1192–1207. Doi https://doi.org/10.1785/0120000916

Jin, Z., & Fialko, Y. (2021). Coseismic and early postseismic deformation due to the 2021 M7. 4 Maduo (China) earthquake. *Geophysical Research Letters*, *48*(21), e2021GL095213. https://doi.org/10.1029/2021gl095213

Kame, N., Rice, J. R., & Dmowska, R. (2003). Effects of prestress state and rupture velocity on dynamic fault branching. *Journal of Geophysical Research*, *108*(B5). https://doi.org/10.1029/2002jb002189

King, G., & Nábělek, J. (1985). Role of fault bends in the initiation and termination of earthquake rupture. *Science*, *228*(4702), 984–987. https://doi.org/10.1126/science.228.4702.984

Klinger, Y. (2010). Relation between continental strike-slip earthquake segmentation and thickness of the crust. *Journal of Geophysical Research*, *115*(B7), B07306. https://doi.org/10.1029/2009jb006550

Leonard, M. (2010). Earthquake fault scaling: Self-consistent relating of rupture length, width, average displacement, and moment release. *Bulletin of the Seismological Society of America*, *100*(5A), 1971–1988. https://doi.org/10.1785/0120090189

Li, Q., Wan, Y., Li, C., Tang, H., Tan, K., & Wang, D. (2022). Source process featuring asymmetric rupture velocities of the 2021 M w 7.4 Maduo, China, earthquake from teleseismic and geodetic data. *Seismological Society of America*, *93*(3), 1429–1439. https://doi.org/10.1785/0220210300

Liu, J., Hu, J., Li, Z., Ma, Z., Wu, L., Jiang, W., et al. (2022). Complete three-dimensional coseismic displacements due to the 2021 Maduo earthquake in Qinghai Province, China from Sentinel-1 and ALOS-2 SAR images. *Science China Earth Sciences*, *65*(4), 687–697. https://doi.org/10.1007/s11430-021-9868-9

Liu, J., Hu, J., Xu, W., Li, Z., Zhu, J., Ding, X., & Zhang, L. (2019). Complete three-dimensional coseismic deformation field of the 2016 central Tottori earthquake by integrating left-and right-looking InSAR observations with the improved SM-VCE method. *Journal of Geophysical Research: Solid Earth*, *124*(11), 12099–12115. https://doi.org/10.1029/2018jb017159

Liu, J.-H., Hu, J., Li, Z.-W., Zhu, J.-J., Sun, Q., & Gan, J. (2017). A method for measuring 3-D surface deformations with InSAR based on strain model and variance component estimation. *IEEE Transactions on Geoscience and Remote Sensing*, *56*(1), 239–250. https://doi.org/10.1109/tgrs.2017.2745576

Lyu, M., Chen, K., Xue, C., Zang, N., Zhang, W., & Wei, G. (2022). Overall subshear but locally supershear rupture of the 2021 Mw 7.4 Maduo earthquake from high-rate GNSS waveforms and three-dimensional InSAR deformation. *Tectonophysics*, *839*, 229542. https://doi.org/10.1016/j.tecto.2022.229542

Meng, L., Inbal, A., & Ampuero, J. P. (2011). A window into the complexity of the dynamic rupture of the 2011 Mw 9 Tohoku-Oki earthquake. *Geophysical Research Letters*, *38*(7). https://doi.org/10.1029/2011gl048118

Michel, R., Avouac, J. P., & Taboury, J. (1999). Measuring ground displacements from SAR amplitude images: Application to the Landers Earthquake. *Geophysical Research Letters*, *26*(7), 875–878. https://doi.org/10.1029/1999GL900138

Poliakov, A. N., Dmowska, R., & Rice, J. R. (2002). Dynamic shear rupture interactions with fault bends and off-axis secondary faulting. *Journal of Geophysical Research*, *107*(B11), ESE6-1–ESE6-18. https://doi.org/10.1029/2001jb000572

Qiu, Q., Hill, E. M., Barbot, S., Hubbard, J., Feng, W., Lindsey, E. O., et al. (2016). The mechanism of partial rupture of a locked megathrust: The role of fault morphology. *Geology*, *44*(10), 875–878. https://doi.org/10.1130/g38178.1

Ren, J., Xu, X., Zhang, G., Wang, Q., Zhang, Z., Gai, H., & Kang, W. (2022). Coseismic surface ruptures, slip distribution, and 3D seismogenic fault for the 2021 Mw 7.3 Maduo earthquake, central Tibetan Plateau, and its tectonic implications. *Tectonophysics*, *827*, 229275. https://doi.org/10.1016/j.tecto.2022.229275

Savage, J. (1965). The stopping phase on seismograms. *Bulletin of the Seismological Society of America*, *55*(1), 47–58. https://doi.org/10.1785/bssa0550010047

Shi, Q., Wei, S., & Chen, M. (2018). An MCMC multiple point sources inversion scheme and its application to the 2016 Kumamoto M w 6.2 earthquake. *Geophysical Journal International*, *215*(2), 737–752. https://doi.org/10.1093/gji/ggy302

Shi, Z., & Day, S. M. (2013). Rupture dynamics and ground motion from 3-D rough-fault simulations. *Journal of Geophysical Research: Solid Earth*, *118*(3), 1122–1141. https://doi.org/10.1002/jgrb.50094

Sieh, K., Jones, L., Hauksson, E., Hudnut, K., Eberhart-Phillips, D., Heaton, T., et al. (1993). Near-field investigations of the landers earthquake sequence. *Science*, *260*(5105), 171–176. April to July 1992. https://doi.org/10.1126/science.260.5105.171

Templeton, E. L., Baudet, A., Bhat, H. S., Dmowska, R., Rice, J. R., Rosakis, A. J., & Rousseau, C. E. (2009). Finite element simulations of dynamic shear rupture experiments and dynamic path selection along kinked and branched faults. *Journal of Geophysical Research*, *114*(B8), B08304. https://doi.org/10.1029/2008jb006174

Wang, M., Wang, F., Jiang, X., Tian, J. B., Li, Y., Sun, J. B., & Shen, Z. K. (2022). GPS determined coseismic slip of the 2021 M w7. 4 Maduo, China, earthquake and its tectonic implication. *Geophysical Journal International*, *228*(3), 2048–2055. https://doi.org/10.1093/gji/ggab460

Wang, S., Song, C., Li, S., & Li, X. (2022). Resolving co-and early post-seismic slip variations of the 2021 M W 7.4 Madoi earthquake in east Bayan Har block with a block-wide distributed deformation mode from satellite synthetic aperture radar data. *Earth and Planetary Physics*, *6*(1), 108–122.

Wang, W., Fang, L., Wu, J., Tu, H., Chen, L., Lai, G., & Zhang, L. (2021). Aftershock sequence relocation of the 2021 Ms7. 4 Maduo earthquake, Qinghai, China. *Science China Earth Sciences*, *64*(8), 1371–1380. https://doi.org/10.1007/s11430-021-9803-3

Wei, S., Fielding, E., Leprince, S., Sladen, A., Avouac, J. P., Helmberger, D., et al. (2011). Superficial simplicity of the 2010 El Mayor-Cucapah earthquake of Baja California in Mexico. *Nature Geoscience*, *4*(9), 615–618. https://doi.org/10.1038/ngeo1213

Wells, D. L., & Coppersmith, K. J. (1994). New empirical relationships among magnitude, rupture length, rupture width, rupture area, and surface displacement. *Bulletin of the Seismological Society of America*, *84*(4), 974–1002.

Wesnousky, S. G. (1988). Seismological and structural evolution of strike-slip faults. *Nature*, *335*(6188), 340–343. https://doi.org/10.1038/335340a0

Wesnousky, S. G. (2006). Predicting the endpoints of earthquake ruptures. *Nature*, *444*(7117), 358–360. https://doi.org/10.1038/nature05275

Wesnousky, S. G. (2008). Displacement and geometrical characteristics of earthquake surface ruptures: Issues and implications for seismic-hazard analysis and the process of earthquake rupture. *Bulletin of the Seismological Society of America*, *98*(4), 1609–1632. https://doi.org/10.1785/0120070111

Yue, H., Shen, Z.-K., Zhao, Z., Wang, T., Cao, B., Li, Z., et al. (2022). Rupture process of the 2021 M7. 4 Maduo earthquake and implication for deformation mode of the Songpan-Ganzi terrane in Tibetan Plateau. *Proceedings of the National Academy of Sciences*, *119*(23), e2116445119. https://doi.org/10.1073/pnas.2116445119

Zeng, H., Wei, S., & Rosakis, A. (2022). A travel-time path calibration strategy for back-projection of large earthquakes and its application and validation through the segmented super-shear rupture imaging of the 2002 Mw 7.9 Denali earthquake. *Journal of Geophysical Research: Solid Earth*, *127*(6), e2022JB024359. https://doi.org/10.1029/2022jb024359

Zeng, H., Wei, S., & Wu, W. (2020). Sources of uncertainties and artefacts in back-projection results. *Geophysical Journal International*, *220*(2), 876–891.

Zhan, Y., Liang, M., Sun, X., Huang, F., Zhao, L., Gong, Y., et al. (2021). Deep structure and seismogenic pattern of the 2021.5. 22 Madoi (Qinghai) M S 7.4 earthquake. *Chinese Journal of Geophysics*, *64*(7), 2232–2252.

Zhang, X., Feng, W., Du, H., Samsonov, S., & Yi, L. (2022). Supershear rupture during the 2021 MW 7.4 Maduo, China, earthquake. *Geophysical Research Letters*, e2022GL097984. https://doi.org/10.1029/2022GL097984

Zhu, L., & Helmberger, D. V. (1996). Intermediate depth earthquakes beneath the India-Tibet collision zone. *Geophysical Research Letters*, *23*(5), 435–438. https://doi.org/10.1029/96gl00385

References From the Supporting Information

Baize, S., Nurminen, F., Sarmiento, A., Dawson, T., Takao, M., Scotti, O., et al. (2020). A worldwide and unified database of surface ruptures (SURE) for fault displacement hazard analyses. *Seismological Research Letters*, *91*(1), 499–520. https://doi.org/10.1785/0220190144

Chen, C. W., & Zebker, H. A. (2002). Phase unwrapping for large SAR interferograms: Statistical segmentation and generalized network models. *IEEE Transactions on Geoscience and Remote Sensing*, *40*(8), 1709–1719. https://doi.org/10.1109/TGRS.2002.802453

Goldstein, R. M., & Werner, C. L. (1998). Radar interferogram filtering for geophysical applications. *Geophysical Research Letters*, *25*(21), 4035–4038. https://doi.org/10.1029/1998gl900033

Gomba, G., Parizzi, A., Zan, F. D., Eineder, M., & Bamler, R. (2016). Toward operational compensation of ionospheric effects in SAR interferograms: The split-spectrum method. *IEEE Transactions on Geoscience and Remote Sensing*, *54*(3), 1446–1461. https://doi.org/10.1109/Tgrs.2015.2481079

Guglielmino, F., Nunnari, G., Puglisi, G., & Spata, A. (2011). Simultaneous and integrated strain tensor estimation from geodetic and satellite deformation measurements to obtain three-dimensional displacement maps. *IEEE Transactions on Geoscience and Remote Sensing*, *49*(6), 1815–1826. https://doi.org/10.1109/TGRS.2010.2103078

Hu, J., Li, Z., Zhu, J., Zhang, L., & Sun, Q. (2012). 3D coseismic Displacement of 2010 Darfield, New Zealand earthquake estimated from multi-aperture InSAR and D-InSAR measurements. *Journal of Geodesy*, *86*(11), 1029–1041. https://doi.org/10.1007/s00190-012-0563-6

Hu, S. W., & Xiao, B. L. (2016). *Modern theory and application of surveying data processing (in Chinese)*. Surveying and Mapping Press.

Jung, H. S., Lu, Z., Won, J. S., Poland, M. P., & Miklius, A. (2011). Mapping three-dimensional surface deformation by combining multiple-aperture interferometry and conventional interferometry: Application to the June 2007 eruption of Kilauea Volcano, Hawaii. *IEEE Geoscience and Remote Sensing Letters*, *8*(1), 34–38. https://doi.org/10.1109/LGRS.2010.2051793

Liu, J., Hu, J., Li, Z., Ma, Z., Wu, L., Jiang, W., et al. (2021). Complete three-dimensional coseismic displacements due to the 2021 Maduo earthquake in Qinghai Province, China from Sentinel-1 and ALOS-2 SAR images. *Science China Earth Sciences*, *65*(4), 687–697. https://doi.org/10.1007/s11430-021-9868-9

Liu, J., Hu, J., Li, Z., Zhu, J. J., Sun, Q., & Gan, J. (2018). A method for measuring 3-D surface deformations with InSAR based on strain model and variance component estimation. *IEEE Transactions on Geoscience and Remote Sensing*, *56*(1), 239–250. https://doi.org/10.1109/TGRS.2017.2745576

Wegmüller, U., Werner, C., Strozzi, T., Wiesmann, A., Frey, O., & Santoro, M. (2016). Sentinel-1 support in the GAMMA software. *Procedia Computer Science*, *100*, 1305–1312. https://doi.org/10.5270/Fringe2015.pp70

Wright, T. J., Parsons, B., England, P. C., & Fielding, E. J. (2004). InSAR observations of low slip rates on the major faults of Western Tibet. *Science*, *305*(5681), 236–239. https://doi.org/10.1126/science.1096388

Zhu, L. P., & Rivera, L. A. (2002). A note on the dynamic and static displacements from a point source in multilayered media. *Geophysical Journal International*, *148*(3), 619–627. https://doi.org/10.1046/j.1365-246x.2002.01610.x